separations

MDPI

Article

A Facile Strategy to Construct Structured Mg-Gallate Adsorbent for Post-Combustion CO_2 Capture Under 80% RH

Siyu Wang, Junyang Du, Junsu Jin * and Jianguo Mi

Beijing Key Laboratory of Membrane Science and Technology, Beijing University of Chemical Technology, Beijing 100029, China

* Correspondence: jinjs@buct.edu.cn

Abstract

Metal–organic frameworks (MOFs) show great potential for post-combustion carbon capture, yet their practical application is often constrained by challenges such as powder handling difficulties, limited structural stability during shaping processes, and performance degradation under high-humidity conditions. In this study, Mg-gallate was structured into millimeter-sized Mg-gallate/CA composite beads via the ionotropic gelation method, and then a hydrophobic layer of vinyltrimethoxysilane (VTMS) was constructed on the bead surface by chemical vapor deposition. The synthesized Mg-gallate/CA and V-Mg-gallate/CA are characterized by XRD, FT-IR, and other techniques, and their CO_2 adsorption behavior, adsorption–desorption kinetics, breakthrough performance, and cyclic stability are systematically evaluated. At 298 K and 0.1 bar, the CO_2 adsorption capacity of Mg-gallate/CA reached 94.2% of that of Mg-gallate powder. The microporous–microporous hierarchical structure constructed by the ionotropic gelation method improved the CO_2 capture efficiency of the composite beads by 16.7% at 0.1 bar. V-Mg-gallate/CA maintained a high dynamic CO_2 adsorption capacity of 2.87 mmol/g for a 10 vol.% CO_2/90 vol.% N_2 gas mixture at 298 K under 80% RH, corresponding to 2.04 times the capacity of Mg-gallate/CA, and retained 98.8% of its initial adsorption capacity at 0.1 bar after 10 cycles. Combining ionotropic gelation shaping with surface hydrophobic modification represents an effective strategy for developing MOF-based adsorbents suitable for post-combustion CO_2 capture.

Keywords: Mg-gallate; ionotropic gelation method; hydrophobic modification; CO_2 adsorption

1. Introduction

The IPCC Sixth Assessment Synthesis Report states that human activities have led to global warming, with the impacts and risks of climate change becoming widespread and evident [1]. Energy consumption has led to a rapid increase in carbon dioxide (CO_2) emissions. Alongside the ongoing energy transition, CO_2 mitigation and recovery represents one of the key technological pathways toward decarbonization [2]. For post-combustion CO_2 capture, existing technologies mainly include absorption [3], adsorption [4], and membrane separation methods [5]. The adsorption method offers advantages such as a relatively simple process flow, lower regeneration energy consumption, and reduced equipment corrosion [6–8]. Common solid adsorbents include zeolites [9], mesoporous silica [10], functionalized amine-based solids [11], and MOFs [12], among others. MOFs are constructed from metal nodes and organic linkers through coordination interactions, offering advantages such as a high specific surface area, tunable pore size, and designable

Check for updates

Academic Editor: Xiong Yang

Received: 10 April 2026
Revised: 6 May 2026
Accepted: 12 May 2026
Published: 14 May 2026

Copyright: © 2026 by the authors. Licensee MDPI, Basel, Switzerland. This article is an open access article distributed under the terms and conditions of the Creative Commons Attribution (CC BY) license.

structural functionality [13–15]. Among the various MOFs, M-gallate has attracted attention due to its suitable micropore size and pore environments rich in oxygen-containing sites [16,17]. Chen et al. demonstrated that M-gallate can synergistically enhance CO_2/N_2 separation through a combination of molecular sieving and polar interactions with the pore walls. Among these materials, Mg-gallate exhibited a particularly outstanding performance, achieving a CO_2 adsorption capacity of 5.05 $mmol \cdot g^{-1}$ at 298 K and 1 bar [18].

However, MOFs are obtained as powders, which pose significant engineering challenges in practical fixed-bed or pressure/temperature swing adsorption processes. Therefore, structuring MOF powders into macroscopic bodies with defined morphology, adequate mechanical strength, and operational stability is an indispensable step for advancing their industrial applications. Existing methods for shaping MOFs mainly include tableting/granulation [19], extrusion [20], spray drying [19], wet granulation/spheronization [21], and 3D printing [22]. Nevertheless, conventional MOF shaping methods still suffer from several drawbacks. High pressure may cause pore collapse, thermal or complex processing may damage crystal integrity, and added binders may dilute active components and block pore channels. Ionotropic gelation is a promising approach in this regard. Using sodium alginate as a gel precursor, MOF powders can be rapidly encapsulated into macroscopic spherical beads through ionic crosslinking with multivalent ions such as Ca^{2+}. This method features mild conditions, simple operation, low equipment requirements, and a tunable particle size [23,24]. In addition, sodium alginate is abundant, inexpensive and non-toxic, while the resulting porous spherical structure is beneficial for mass transfer and a practical fixed-bed application [25].

The humidity in actual flue gas is extremely high; water vapor tends to occupy polar sites first and competes with CO_2 for adsorption, while sodium calcium alginate itself is highly hydrophilic and is more prone to accumulating moisture in high-humidity flue gas. To enhance the carbon dioxide adsorption capacity of structured adsorbent under high-humidity conditions, a hydrophobic barrier was constructed on their surfaces. Chemical vapor deposition (CVD) requires minimal solvents, produces a uniform coating, and involves a gentle process that minimizes the impact on the pore structure [26,27].

In this study, Mg-gallate was used as the active component for CO_2 adsorption, structured adsorbent microspheres were prepared by ionotropic gelation, and a VTMS coating was deposited on the particle surface by chemical vapor deposition to achieve hydrophobic modification. A series of characterization results confirmed that the crystal structure remained intact after structuring and hydrophobic modification. The mass-transfer behavior and dynamic separation performance of the adsorbent were evaluated through adsorption/desorption kinetics and simulated flue-gas breakthrough experiments under dry and 80% RH conditions. This study aims to develop a structured MOF adsorbent that integrates a high CO_2 adsorption capacity, efficient mass transfer, and moisture resistance, thereby providing a new strategy for promoting the application of structured MOF adsorbents in flue-gas CO_2 capture.

2. Materials and Methods

2.1. Reagents

The monodisperse nano-magnesium-oxide dispersion (MgO), sodium alginate (SA), calcium chloride dihydrate ($CaCl_2 \cdot 2H_2O$), and vinyltrimethoxysilane (VTMS) were purchased from Macklin Biochemical Technology Co., Ltd., Shanghai, China, while gallic acid (H_4gel) was obtained from Aladdin Biochemical Technology Co., Ltd., Shanghai, China. All reagents were used without further purification.

2.2. Synthesis of Samples

2.2.1. Preparation of Mg-Gallate/CA Composite Beads

A total of 4 g of Mg-gallate powder was dispersed in deionized water and sonicated to ensure thorough mixing; then, 6 wt.% sodium alginate was added, and the mixture was stirred at room temperature for 2 h. The mixture was drawn into a 10 mL syringe, and the beads dispensed into $CaCl_2$ solution to gel. After a certain period, washing was carried out with deionized water, drying was carried out at 333 K, and Mg-gallate/CA composite beads were obtained.

2.2.2. Hydrophobic Modification

Hydrophobic modification of Mg-gallate/CA was performed using chemical vapor deposition. A total of 0.1 g of VTMS was placed in a Petri dish and covered with a layer of perforated aluminum foil. A total of 0.1 g of the beads was added, and the entire assembly was heated in an oven at 403 K for 1 h to complete the hydrophobic coating. After cooling to room temperature, the hydrophobic-coated spheres were obtained and named V-Mg-gallate/CA composite beads, as shown in Figure 1.

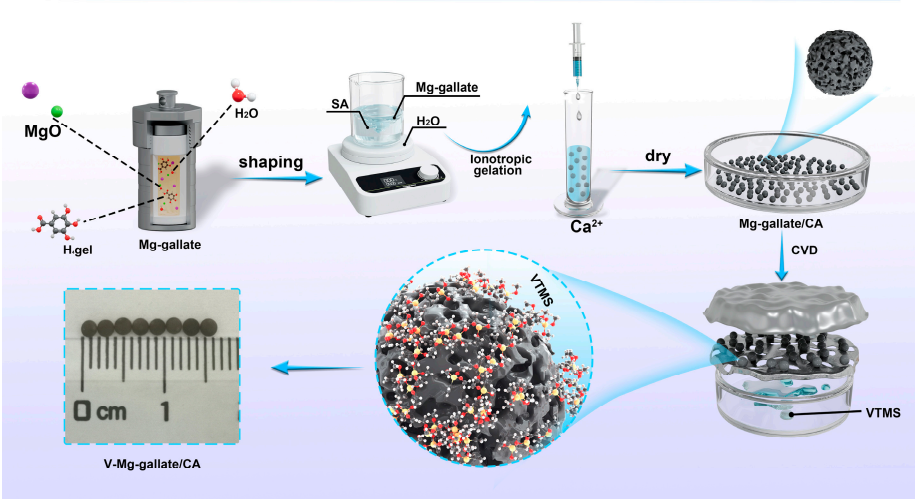


Figure 1. Diagram of preparation process for V-Mg-gallate/CA composite beads.

2.3. Characterization Methods

Detailed characterization methods are provided in the Supporting Information, including X-ray diffraction (XRD), Fourier-transform infrared spectra (FT-IR), scanning electron microscopy (SEM), X-ray photoelectron spectroscopy (XPS), specific surface area and pore size analysis, Thermogravimetric analysis (TGA), water contact angle.

2.4. Performance Test Methods

2.4.1. Single-Component Adsorption Performance Test

CO_2 and N_2 adsorption measurements were conducted using a surface area and pore size analyzer (JW-BK122W, JWGB, Beijing, China). All samples were pretreated at 403 K for 12 h to remove impurities. The adsorption temperature was controlled by a constant-temperature water bath.

For the water adsorption test, samples were first degassed at 403 K for 12 h and then placed in a glass desiccator containing a saturated KCl solution [28]. The change in sample mass before and after 24 h exposure to water vapor was subsequently measured.

2.4.2. Adsorption–Desorption Kinetic Performance Test

CO_2 adsorption/desorption kinetics of the samples were measured using a gravimetric dynamic adsorption analyzer (VVS, BSD, Beijing, China). The samples were activated under vacuum at 403 K for 12 h. Adsorption was then carried out under a 10 vol.% CO_2/90 vol.% N_2 mixture, while desorption was performed by purging with N_2 at 403 K.

2.4.3. Multi-Component Breakthrough Adsorption Performance Test

Competitive adsorption experiments were conducted using a multi-component breakthrough curve analyzer (BSD-MAB, Beijing, China) with a CO_2/N_2 gas mixture. Approximately 1.0 g of the sample was loaded into the adsorption column and activated at 403 K for 6 h. The mass transfer length is approximately 14 cm. During the test, the total gas mixture of 10 vol.% CO_2/90 vol.% N_2 was injected into the adsorbent bed with a total flow rate of 4 sccm. Breakthrough curves under 80% RH were similarly determined using the test method described above.

2.4.4. Cyclic Stability Test

To evaluate the cyclic adsorption stability of the samples, multiple CO_2 adsorption cycles were conducted using a gas adsorption analyzer. The samples were degassed under vacuum at 403 K for 2 h to thoroughly remove pre-adsorbed moisture and other impurity molecules from the pores. CO_2 adsorption performance was measured at 298 K. After each adsorption test, the samples were degassed under vacuum at 403 K for 30 min to achieve complete desorption of the adsorbate and recover the accessible adsorption sites, and then the next cyclic test was performed.

2.5. Model Fitting

The Dual-Site Langmuir–Freundlich (DSLF) model [29] is primarily used to describe complex adsorption systems with heterogeneous adsorption sites characterized by two distinct energy distributions. Its equation is expressed as follows:

$$q = \frac{q_{m1}(b_1 p)^{n_1}}{1 + (b_1 p)^{n_1}} + \frac{q_{m2}(b_1 p)^{n_2}}{1 + (b_2 p)^{n_2}}$$

where q (mmol/g) is the adsorption capacity; q_{m1} and q_{m2} (mmol/g) are the maximum adsorption capacities of the two sites; b_1 and b_2 are the affinity constants of the two sites; n_1 and n_2 are the heterogeneity indices of the two sites; and p (bar) is the pressure.

2.6. Isosteric Heat of Adsorption Calculation

The Clausius–Clapeyron equation [30], expressed as follows, is used to calculate the isosteric heat of adsorption:

$$\frac{Q_{st}}{R} = \left(\frac{\partial ln p}{\partial \left(\frac{1}{T} \right)} \right)_q$$

where Q_{st} (kJ/mol) is the isosteric heat of adsorption; R is the universal gas constant, 8.314 J/(mol·K); T (K) is the absolute temperature; and p (bar) is the equilibrium pressure.

3. Results

3.1. Characterization Results

The XRD patterns (Figure 2a) reveal that all samples display peaks at 11.40°, 14.02°, and 24.46° corresponding to Mg-gallate, which are in good agreement with previously reported peak positions [16]. From the FT-IR spectra (Figure 2b), both Mg-gallate, Mg-gallate/CA and V-Mg-gallate/CA exhibit the asymmetric and symmetric stretching vi-

brations of the carboxylate group (COO^-) from the ligand at 1627 cm^{-1} and 1377 cm^{-1}, respectively. The peak at 751 cm^{-1} corresponds to the vibration of the aromatic ring in the ligand [16]. This indicates that Mg-gallate was successfully immobilized within the CA network, while the hydrophobic modification preserved its crystal structure. In the spectrum of Mg-gallate/CA, the characteristic peaks of CA are not observable. This may be attributed to two factors: firstly, the relatively low addition amount of sodium alginate; secondly, the possible intermolecular interactions between CA and Mg-gallate may exist. In the XPS spectra of Mg-gallate/CA (Figure 2c), no Na 1s signal is detected at a binding energy of 1071 eV, whereas a strong Ca 2p peak is observed, exhibiting the characteristic spin–orbit splitting into Ca $2p_3/_2$ (346.8 eV) and Ca $2p_1/_2$ (350.6 eV) components (Figure 2d) [31]. This indicates that Na^+ ions from the sodium alginate precursor were completely exchanged during the Ca^{2+} crosslinking process. Therefore, as is shown in Figure S1, the weak feature at 350.8 eV of Mg-gallate should not be assigned to Ca 2p. This peak is likely attributable to impurities or background noise. In the FT-IR spectrum of V-Mg-gallate/CA, a weak shoulder appears on the right side of the peak at 1059 cm^{-1} corresponding to the Si-O-Si stretching vibrations from VTMS species [32]. Meanwhile, its EDS spectrum shows peaks of Si 2s and Si 2p at 152.1 eV and 101.1 eV, respectively. Further analysis of the Si spectrum revealed the Si-C bond at 100.8 eV, the Si-O bond at 101.6 eV and the Si-O-Si bond at 102.3 eV (Figure S2). These indicate that VTMS has been successfully deposited onto the surface of the composite beads. CA is entirely hydrophilic, while the water contact angles of Mg-gallate and Mg-gallate/CA are 35° and 47°, respectively. After hydrophobic modification, the water contact angle of Mg-gallate/CA increased from being completely hydrophilic to 135° (Figure S3). The water uptake of Mg-gallate/CA and V-Mg-gallate/CA was 3.41 and 1.62 mmol/g, respectively, indicating that the hydrophobic modification effectively reduced water adsorption. The mechanical strength of Mg-gallate/CA and V-Mg-gallate/CA was 9.72 N and 9.68 N, respectively, indicating that the hydrophobic modification did not compromise the compressive stability of the beads.

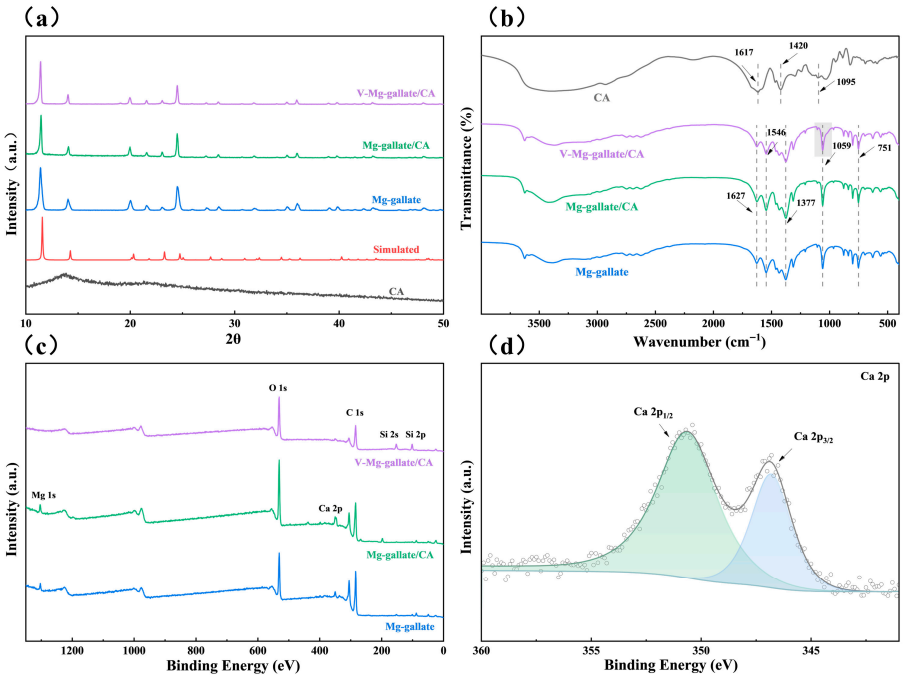


Figure 2. (**a**) XRD patterns, (**b**) FT-IR spectra, (**c**) XPS survey spectra of the samples, and (**d**) Ca 2p XPS spectrum of Mg-gallate/CA.

Scanning electron microscopy (SEM) was employed to characterize the morphology of the samples. Figure 3a shows the microstructure of the synthesized Mg-gallate crystal pow-

der, which is in good agreement with previously reported morphologies [17]. As is shown in Figure 3b, Mg-gallate/CA composite beads exhibited a regular spherical morphology with a particle size of approximately 0.2 mm. The EDS mapping images of Mg-gallate/CA (Figure S4) revealed that the four characteristic elements (C, O, Mg, and Ca) were uniformly distributed across the surface of the composite bead. The atomic percentage of Na on the bead surface was zero, while the Ca content was 1.14% (Figure S5). This confirms that a thorough ion-exchange reaction occurred during the gelation process. Figure 3c presented the cross-sectional microstructure of Mg-gallate/CA composite beads. Calcium alginate formed a honeycomb-shaped porous network gel structure, creating highly open mass transfer channels. In the surface EDS mapping images of V-Mg-gallate/CA composite beads (Figure 3d), the uniform distribution of Si indicates successful deposition of VTMS, while the Si content is 1.23% (Figure S6). As is shown in Figure S7, the uniform distribution of Si across the cross-section of V-Mg-gallate/CA indicates that, during chemical vapor deposition, Si diffused into the interior of the support through the pore channels. However, the Si content was lower than that on the surface (Figure S8).

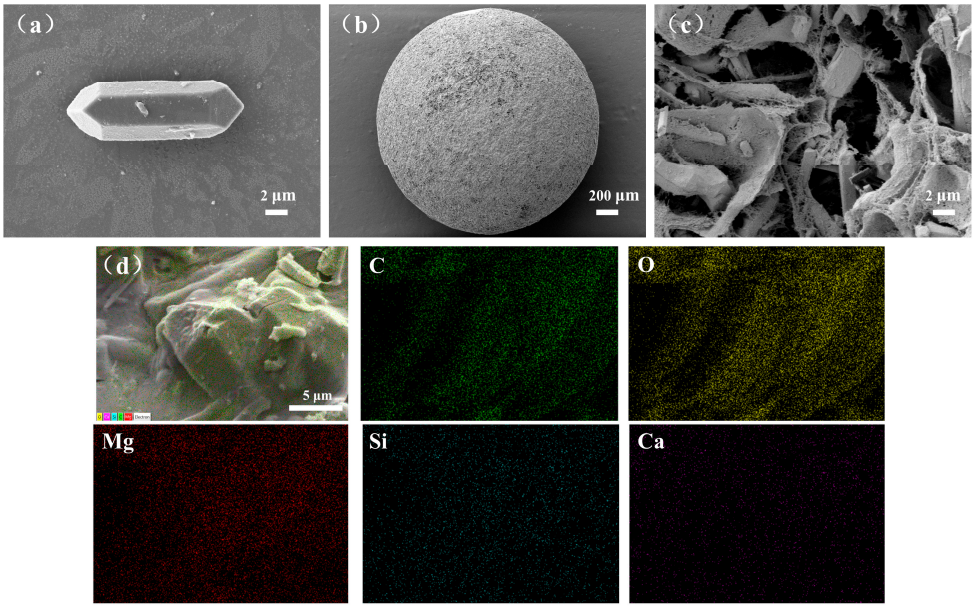


Figure 3. SEM images. (**a**) Mg-gallate powder; Mg-gallate/CA: (**b**) overall morphology, (**c**) cross-sectional morphology; (**d**) EDS mapping images of C, O, Mg, Si, Ca elements in V-Mg-gallate/CA.

According to TGA curves shown in Figure S9, neither the ionotropic gelation process nor the hydrophobic modification affected the thermal stability of Mg-gallate. However, in the second stage of thermal decomposition, the weight-loss curves of Mg-gallate/CA and V-Mg-gallate/CA are slightly lower than that of Mg-gallate. This can be attributed to the cleavage of glycosidic bonds and the decomposition of the carbon chain backbone in the calcium alginate macromolecular chains [33].

The N_2 adsorption–desorption isotherms of Mg-gallate and Mg-gallate/CA were measured at 77 K and are shown in Figure 4a,b. Mg-gallate/CA exhibits adsorption behavior Type I isotherms, similar to that of Mg-gallate, indicating that its microporous structure was retained. Compared with Mg-gallate, the specific surface area of Mg-gallate/CA decreased (Table 1), due to dilution of the active adsorbent component by the addition of the binder. As is shown in Figure 4c, Mg-gallate/CA shows a pronounced peak in the pore-size distribution at 2.89 μm, confirming the dominance of macropores. This confirms the presence of a microporous–microporous hierarchical structure in the composite, consisting of macropores derived from the gel network and micropores of Mg-gallate, which is generally favorable for mass transfer. Compared with Mg-gallate, the hysteresis in the N_2 adsorption/desorption

isotherm of Mg-gallate/CA at 77 K was significantly alleviated. The hysteresis observed for Mg-gallate may be attributed to the restricted diffusion of N_2 in narrow micropores at low temperatures, together with the presence of flexible pore channels. After structuring by ionotropic gelation, Mg-gallate/CA developed a macropore–micropore hierarchical structure, which effectively reduced powder aggregation and improved the accessibility of the pore network to gas molecules. Consequently, the mass-transfer resistance during both adsorption and desorption was lowered, leading to a weakened hysteresis behavior.

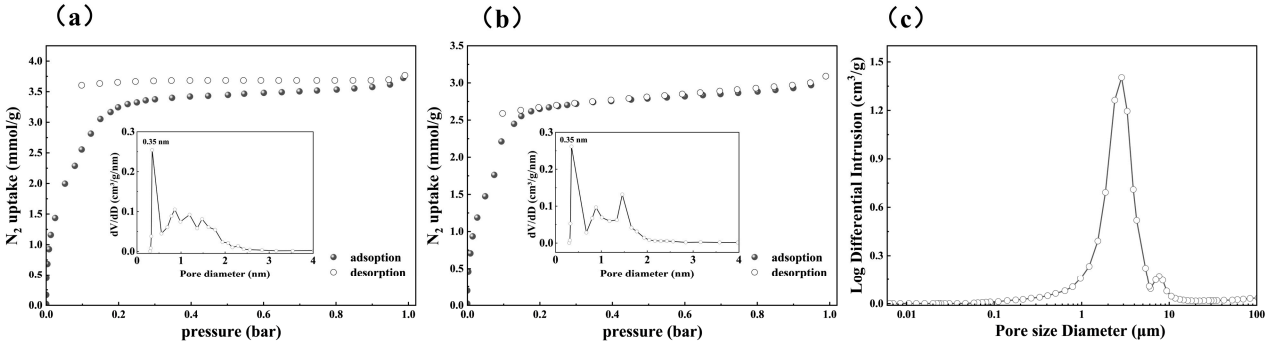


Figure 4. N_2 adsorption–desorption isotherms at 77 K and corresponding NLDFT pore size distributions of (**a**) Mg-gallate and (**b**) Mg-gallate/CA; (**c**) pore size distribution of Mg-gallate/CA measured by mercury intrusion porosimetry.

Table 1. Structural properties of Mg-gallate and Mg-gallate/CA.

Sample	S_{BET} (m^2/g)	$S_{Langmuir}$ (m^2/g)	V (m^3/g)	Pore Size (nm)
Mg-gallate	287.79	407.48	0.12	1.77
Mg-gallate/CA	242.06	305.45	0.10	1.76

3.2. Single-Component Adsorption Performance

Single-component adsorption performance was evaluated by measuring CO_2 and N_2 adsorption at different temperatures (Figure 5). At 298 K and 0.1 bar, Mg-gallate/CA exhibited a CO_2 adsorption capacity of 4.42 mmol/g, which corresponds to 94.2% of that of Mg-gallate powder (4.69 mmol/g, Figure S10a), and is consistent with the mass fraction of powder in the composite bends. Mg-gallate/CA displays a typical gate-opening behavior characterized by an S-shaped adsorption isotherm, showing a two-step adsorption profile [34]. At low CO_2 pressures, the pore channels of Mg-gallate/CA remain closed, preventing CO_2 molecules from entering. As the CO_2 partial pressure increases, the pores open and allow a large number of CO_2 molecules to enter, causing a sharp increase in adsorption capacity. Following this, the CO_2 uptake reaches a plateau, and further increases in CO_2 partial pressure do not lead to an additional adsorption rise. As the adsorption temperature increases, the threshold pressure for the gate-opening shifts to higher values. This is because the thermodynamic stability of the high CO_2 loading state in Mg-gallate/CA decreases with increasing temperature, raising the critical chemical potential required to trigger the gate-opening effect [35]. Moreover, Mg-gallate/CA exhibits negligible N_2 adsorption, making it highly suitable for CO_2/N_2 separation applications shown in Figure 5b.

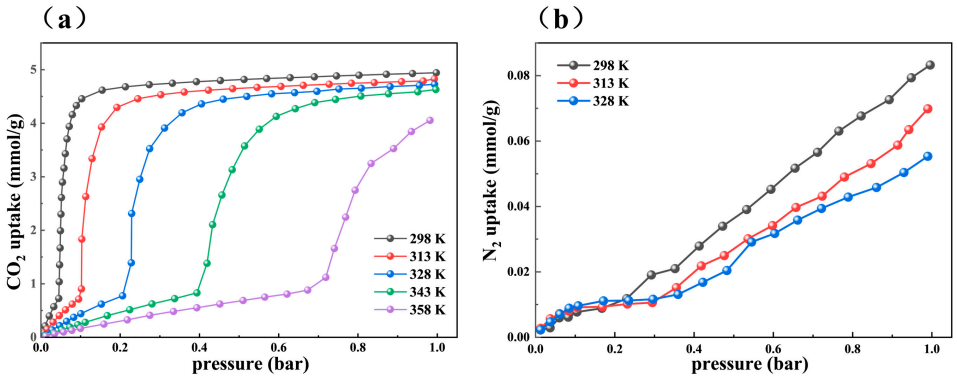


Figure 5. CO_2 (**a**) and N_2 (**b**) adsorption isotherms of Mg-gallate/CA at different temperatures.

To evaluate the adsorption affinity of Mg-gallate/CA toward CO_2 and N_2, as well as its thermodynamic characteristics, adsorption isotherms obtained at the temperature range of 298 K to 328 K were fitted to the DSLF adsorption isotherm model. As is shown in Table S1, the three fitted curves exhibit correlation coefficients of $R^2 > 0.99$, indicating that the DSLF model can satisfactorily describe the adsorption isotherms. The isosteric heat of adsorption was subsequently calculated using the Clausius–Clapeyron equation. The average isosteric heat of adsorption for CO_2 on Mg-gallate/CA was 39.6 kJ/mol. The gate-opening effect does not influence the isosteric heat of adsorption, which remains relatively constant with increasing uptake. Compared with other flexible MOFs such as In-MIL-53D (24.1 kJ/mol) [36] and ZnDatzBdc (26–34.5 kJ/mol) [37], the value is higher, yet still within the range of physisorption. For Mg-gallate/CA, the CO_2 affinity is mainly associated with the polar oxygen-containing sites from gallate ligands. As is shown in Table 2, compared with other MOF powders and structured adsorbents, Mg-gallate/CA and V-Mg-gallate/CA exhibit superior CO_2 adsorption performance at 0.1 bar and 298 K and relatively low heats of adsorption. The isosteric heat of adsorption for N_2 ranged from 2 to 10 kJ/mol (Figure 6c), which is significantly lower than that for CO_2, indicating a weaker affinity of Mg-gallate/CA toward N_2. This makes it suitable for CO_2/N_2 separation applications. To further evaluate the fitting performance of the adsorption model, the residual was calculated. As is shown in Figures S12 and S13, the residuals were mainly distributed around zero and showed no obvious systematic trend, indicating that the DSLF model can reasonably describe the CO_2 and N_2 adsorption behavior of Mg-gallate/CA. In addition, the root mean square error (RMSE) values were further calculated (Tables S1 and S2), and the relatively low RMSE values indicate that the model provides good fitting reliability.

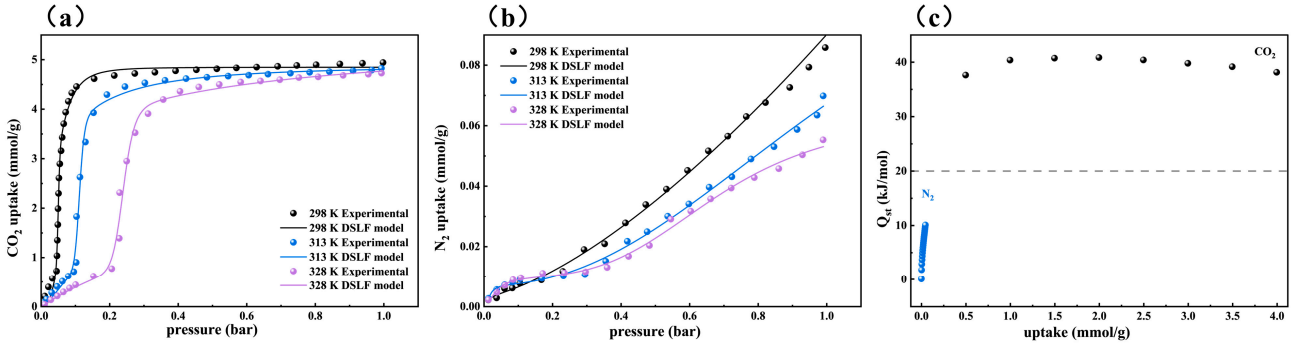


Figure 6. CO_2 (**a**) and N_2 (**b**) adsorption isotherms of Mg-gallate/CA at 298–328 K with model fitting, and (**c**) the corresponding isosteric heats of adsorption.

Table 2. Comparison of CO_2 adsorption performance between Mg-gallate/CA and other reported adsorbents.

Adsorbents	Shape	CO_2 Uptake (mmol/g, 298 K)		Q_{st} (kJ/mol)	References
		0.1 bar	1 bar		
Mg-gallate	Powder	1.5	5.05	37	[18]
Mg/DOBDC	Powder	1.20	5.45	47.5	[38]
mmen-Mg_2dobpdc	Powder	3.5	4.1	71	[39]
CALF-20	Powder	2.5 [a]	4.0 [a]	38–41	[40]
In-MIL-53D	Powder	-	1.43	24.1	[36]
ZnDatzBdc	Powder	0.22	5.41	26–34.5	[37]
UiO-66@PAN10	Sphere	0.32	2.0	34.3–35.3	[41]
ZIF-8@PAN10	Sphere	0.2	1.0	22.9–24.4	[41]
Ni(3-ain)$_2$ pellets	Pellet	0.94	2.9	-	[42]
DB67M-HC-DETA	Pellet	0.8	1.9	-	[43]
TEPA-MIL-101M_B	Honeycomb	2.0	2.6	-	[44]
Fe-MOR(0.25)	Extrudate	3.07	3.89	10–40	[45]
ALF@poly(acrylates)-F	Sphere	1.8	4.2	38.8	[46]
Mg-gallate/CA	Sphere	4.42	4.94	39.6	This study
V-Mg-gallate/CA	Sphere	3.94	4.77	-	This study

[a] Adsorption temperature 293 K.

3.3. Adsorption–Desorption Kinetic Performance

Intrinsic adsorption–desorption kinetics of Mg-gallate and Mg-gallate/CA were evaluated using a 10 vol.% CO_2/90 vol.% N_2 gas mixture. As is shown in Figure 7, Mg-gallate powder and Mg-gallate/CA required 14.5 min and 14.0 min to reach 90% of its equilibrium CO_2 adsorption capacity, and took 11.5 min and 7.0 min to achieve 90% desorption. The CO_2 adsorption capacity of Mg-gallate in a single adsorption cycle (based on a 90% adsorption–desorption capacity) was 3.22 mmol/g, while that of Mg-gallate/CA was 3.02 mmol/g. The CO_2 capture efficiency was 0.14 mmol/g/min for Mg-gallate/CA, compared to 0.12 mmol/g/min for Mg-gallate, representing a 16.7% improvement. The shortened adsorption–desorption time improved process efficiency, which can be attributed to the macropore–micropore coupled structure formed by ionotropic gelation, where the macroporous network and the intrinsic micropores of Mg-gallate crystals jointly promoted CO_2 mass transfer.

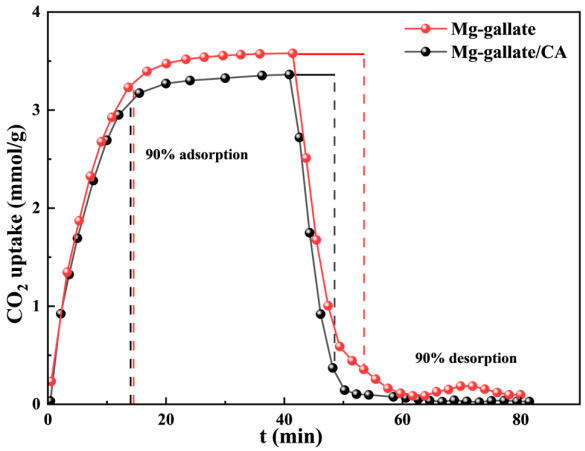


Figure 7. CO_2 adsorption–desorption kinetic curves of Mg-gallate and Mg-gallate/CA using 10 vol.% CO_2/90 vol.% N_2 gas mixture at 298 K (the dashed lines represent the time required for CO_2 to reach 90% adsorption saturation and 90% desorption completion).

3.4. Dynamic Breakthrough Test

Multi-component breakthrough tests were conducted to evaluate the dynamic separation performance of the samples with a 10 vol.% CO_2/90 vol.% N_2 gas mixture at 298 K under dry atmosphere. N_2 broke through shortly after introduction of the gas mixtures, indicating its negligible uptake in Mg-gallate and Mg-gallate/CA. Nevertheless, CO_2 breakthrough occurred at 41 and 47 min for Mg-gallate and Mg-gallate/CA, respectively. The CO_2-breakthrough time delay indicates that Mg-gallate/CA can retain CO_2 for a longer period in the fixed bed and improved CO_2 separation performance. The dynamic CO_2 adsorption capacity of Mg-gallate powder was 3.53 mmol/g (Figure S11), while that of Mg-gallate/CA was 3.40 mmol/g (Figure 8a), representing only a 3.7% decrease compared to Mg-gallate powder under dry condition. This indicates that the ionotropic gelation shaping process did not significantly compromise the CO_2 adsorption performance of Mg-gallate, and the microporous–microporous hierarchical structure of the gel network within Mg-gallate/CA facilitates gas flow pathways and reduces mass transfer resistance, allowing CO_2 molecules to more effectively access and diffuse to the adsorption active sites. It is noted that the dynamic selectivity values for Mg-gallate and Mg-gallate/CA were 515 and 401, respectively. The hydrophobically modified V-Mg-gallate/CA exhibited a dynamic CO_2 adsorption capacity of 2.92 mmol/g under dry conditions (Figure 8c), retaining 85.9% of the capacity of Mg-gallate/CA, and breakthrough occurred at 45 min. This decrease in adsorption capacity suggests that the introduction of the hydrophobic layer partially occupies accessible pores or surface sites to some extent.

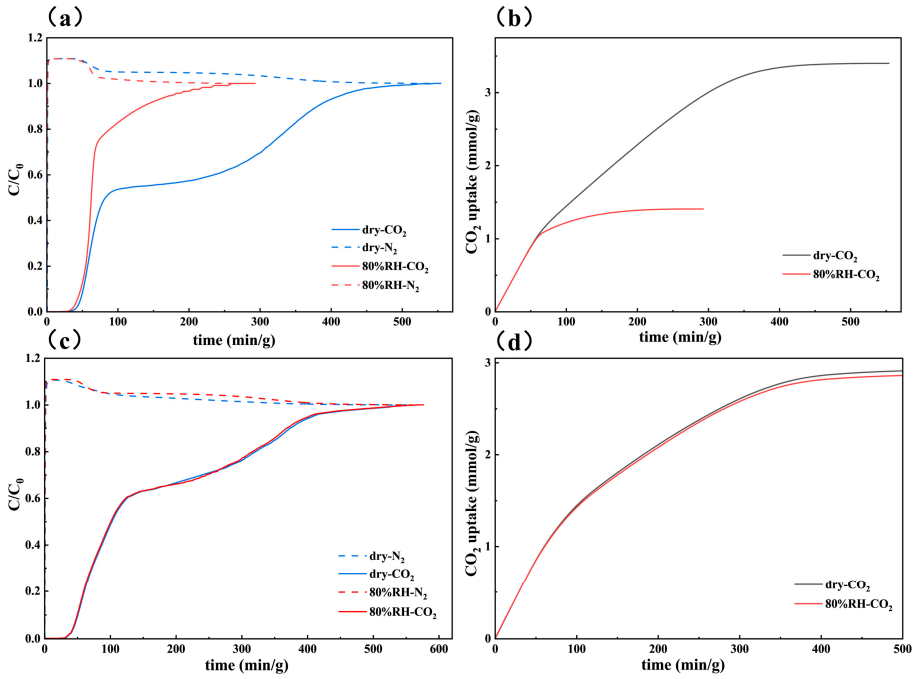


Figure 8. Breakthrough curves of (**a**) Mg-gallate/CA and (**c**) V-Mg-gallate/CA for 10 vol.% CO_2/90 vol.% N_2 gas mixture at 298 K under 0% RH and 80% RH; (**b**) time-dependent CO_2 adsorption curves of Mg-gallate/CA and (**d**) V-Mg-gallate/CA.

To delve deeper into the effect of water vapor on the CO_2 adsorption performance of Mg-gallate/CA and V-Mg-gallate/CA, we conducted tests using 10 vol.% CO_2/90 vol.% N_2 under 80% RH. The dynamic CO_2 adsorption capacity of Mg-gallate/CA was only 1.41 mmol/g (Figure 8a), representing a loss of 58.5% compared to dry conditions. In contrast, V-Mg-gallate/CA exhibited a dynamic CO_2 adsorption capacity of 2.87 mmol/g under 80% RH (Figure 8d), corresponding to 2.04 times the capacity of Mg-gallate/CA. This indicates that the VTMS hydrophobic layer effectively inhibits the adsorption and

accumulation of water molecules on the composite beads' surface, reducing the competitive occupation of CO_2 adsorption sites by water vapor and mitigating pore blocking effects. As a result, V-Mg-gallate/CA retains a favorable dynamic separation performance for post-combustion CO_2 adsorption under 80% RH.

3.5. Cyclic Stability

The cyclic stability test of adsorbents is primarily used to evaluate the ability to maintain adsorption capacity, the stability of active sites, and structural durability over multiple adsorption–desorption regeneration cycles. After 10 adsorption–desorption cycles at 298 K, Mg-gallate/CA and V-Mg-gallate/CA retained 94.1% and 98.8% of their initial adsorption capacity at 0.1 bar, respectively (Figure 9), indicating that hydrophobic coating enhances the cyclic stability of Mg-gallate/CA. The water contact angle of V-Mg-gallate/CA decreased to 131° after 10 cycles (Figure S3e), indicating that repeated cycling led to a loss of hydrophobicity.

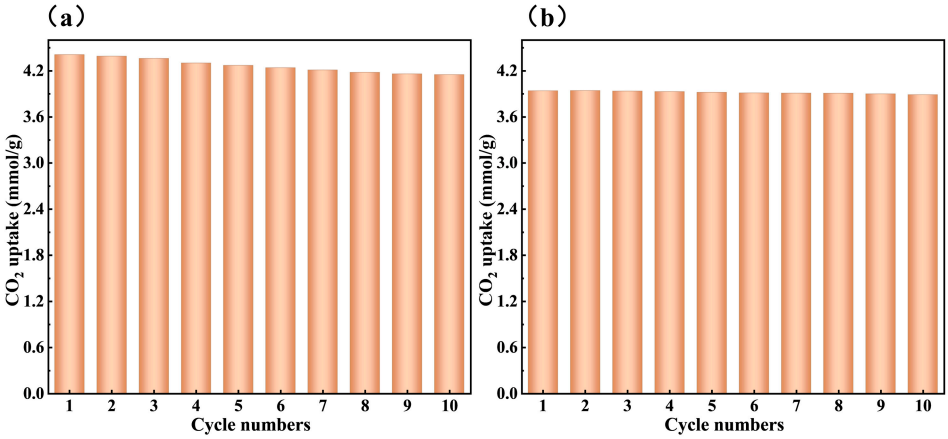


Figure 9. Cyclic stability of (**a**) Mg-gallate/CA and (**b**) V-Mg-gallate/CA.

4. Conclusions

In summary, the ionotropic gelation method enables the macroscopic structuring of Mg-gallate while preserving its original crystal structure and adsorption properties, and enhances its mass transfer performance. Mg-gallate/CA exhibited a CO_2 adsorption capacity of 4.42 mmol/g at 298 K and 0.1 bar, corresponding to 94.2% of that of the pristine powder, indicating that the shaping process did not cause significant capacity loss. Meanwhile, the adsorption–desorption cycle time was shortened from 26 min for the pristine powder to 21 min for the composite, and the CO_2 capture efficiency increased by 16.7%, indicating that the microporous–microporous hierarchical structure constructed by ionotropic gelation effectively promoted gas diffusion and mass transfer. The introduction of a VTMS hydrophobic layer significantly enhanced the adaptability to humid simulated flue gas. Notably, the water contact angles of Mg-gallate and Mg-gallate/CA were 35° and 47°, respectively. In contrast, following hydrophobic modification, V-Mg-gallate/CA displays hydrophobic behavior, as evidenced by a water contact angle of 135°. Consequently, the adsorption performance of the composite beads in humid simulated flue gas is enhanced, with V-Mg-gallate/CA exhibiting a dynamic adsorption capacity of 2.04 times that of Mg-gallate/CA. After 10 cycles, the capacity retention rates of Mg-gallate/CA and V-Mg-gallate/CA reached 94.1% and 98.8% respectively, demonstrating preliminary cyclic stability. Therefore, the combination of ionotropic gelation shaping and surface hydrophobic modification offers a viable pathway for facilitating the application of MOF-based adsorbents from humid post-combustion CO_2 capture.

Supplementary Materials: The following supporting information can be downloaded at: https://www.mdpi.com/article/10.3390/separations13050148/s1, Figure S1: The feature at 350.8 eV XPS spectrum of Mg-gallate; Figure S2: Si 2p XPS spectrum of V-Mg-gallate/CA; Figure S3: Water contact angles of CA (a), Mg-gallate (b), Mg-gallate/CA (c), V-Mg-gallate/CA (d) and V-Mg-gallate/CA after ten cycles (e); Figure S4: Elemental mapping images of Mg-gallate/CA; Figure S5: EDS surface elemental mapping of Mg-gallate/CA.; Figure S6: EDS surface elemental mapping of V-Mg-gallate/CA; Figure S7: Elemental mapping images of cross-section of V-Mg-gallate/CA; Figure S8: EDS surface elemental mapping of cross-section of V-Mg-gallate/CA; Figure S9: TGA curves of Mg-gallate, Mg-gallate/CA and V-Mg-gallate/CA; Figure S10: CO_2 adsorption isotherm of Mg-gallate (a), V-Mg-gallate/CA (b), and CA (c) at 298 K; Figure S11: Breakthrough curves of (a) Mg-gallate for 10 vol.% CO_2/90 vol.% N_2 gas mixture at 298 K; (b) time-dependent CO_2 adsorption curves of Mg-gallate; Figure S12: Fitting residual plot for CO_2 adsorption isotherms of Mg-gallate/CA; Figure S13: Fitting residual plot for N_2 adsorption isotherms of Mg-gallate/CA; Table S1: Fitting parameters for CO_2 adsorption isotherms of Mg-gallate/CA; Table S2: Fitting parameters for N_2 adsorption isotherms of Mg-gallate/CA.

Author Contributions: Conceptualization, S.W.; methodology, S.W. and J.J.; formal analysis, S.W. and J.D.; resources, S.W. and J.J.; data curation, S.W. and J.D.; writing—original draft preparation, S.W.; writing—review and editing, S.W., J.D. and J.J.; supervision, J.J. and J.M.; funding acquisition, J.J. and J.M. All authors have read and agreed to the published version of the manuscript.

Funding: This research was funded by Joint Key Program of National Natural Science Foundation of China (U22B20147).

Data Availability Statement: The original contributions presented in this study are included in the article or Supplementary Materials. Further inquiries can be directed to the corresponding author.

Conflicts of Interest: The authors declare no conflicts of interest.

References

1. Calvin, K.; Dasgupta, D.; Krinner, G.; Mukherji, A.; Thorne, P.W.; Trisos, C.; Romero, J.; Aldunce, P.; Barrett, K.; Blanco, G.; et al. *IPCC, 2023: Climate Change 2023: Synthesis Report. Contribution of Working Groups I, II and III to the Sixth Assessment Report of the Intergovernmental Panel on Climate Change*; Core Writing Team, Lee, H., Romero, J., Eds.; Intergovernmental Panel on Climate Change (IPCC): Geneva, Switzerland, 2023.
2. IEA. CCUS in Clean Energy Transitions—Analysis. Available online: https://www.iea.org/reports/ccus-in-clean-energy-transitions (accessed on 1 April 2026).
3. Gómez-Díaz, D.; Navaza, J.M.; Rumbo, A. Carbon Dioxide Chemical Absorption Using Diamines with Different Types of Active Centers. *Separations* **2022**, *9*, 343. [CrossRef]
4. Radić, N.; Nastasović, A.; Tadić, T.; Vuković, Z.; Krstić, J.; Marković, B. Tetraethylenepentamine-Grafted Magnetic Polymer Composite as Promising Sorbent for CO_2 Capture. *Separations* **2026**, *13*, 56. [CrossRef]
5. Checchetto, R. Polyethylene Glycol (PEG) Additive in Polymer Membranes for Carbon Dioxide Separation: A Critical Review on Performances and Correlation with Membrane Structure. *Separations* **2025**, *12*, 71. [CrossRef]
6. Ren, L.; Cheng, S.; Xie, T.; Zhang, Q.; Li, R.; Yue, T.; Cai, C. Low-Energy Regeneration Technologies for Industrial CO_2 Capture: Advances, Challenges, and Engineering Applications. *Sustainability* **2025**, *17*, 9796. [CrossRef]
7. Wang, Y.; Tang, X.; Yi, H. Adsorption Materials for Carbon Capture: Research Advancements and Prospects. *Separations* **2025**, *12*, 334. [CrossRef]
8. Obi, D.; Onyekuru, S.; Orga, A. Review of Recent Process Developments in the Field of Carbon Dioxide (CO_2) Capture from Power Plants Flue Gases and the Future Perspectives. *Int. J. Sustain. Energy* **2024**, *43*, 2317137. [CrossRef]
9. Tao, Z.; Tian, Y.; Wu, W.; Liu, Z.; Fu, W.; Kung, C.-W.; Shang, J. Development of Zeolite Adsorbents for CO_2 Separation in Achieving Carbon Neutrality. *npj Mater. Sustain.* **2024**, *2*, 20. [CrossRef]
10. Tumurbaatar, O.; Popova, M.; Mitova, V.; Shestakova, P.; Koseva, N. Engineering of Silica Mesoporous Materials for CO_2 Adsorption. *Materials* **2023**, *16*, 4179. [CrossRef] [PubMed]
11. Hack, J.; Maeda, N.; Meier, D.M. Review on CO_2 Capture Using Amine-Functionalized Materials. *ACS Omega* **2022**, *7*, 39521–39530. [CrossRef] [PubMed]

12. Kari, N.E.F.; Ismail, M.; Ahmad, A.; Kamal, K.; Chew, T.L.; Bustam, M.A. Screening and Experimental Validation for Selection of Open Metal Sites Metal-Organic Framework (M-CPO-27, M = Co, Mg, Ni and Zn) to Capture CO_2. *Separations* **2023**, *10*, 434. [CrossRef]
13. Zhao, Z.; Nie, J.; Huang, H.; He, F.; Wang, K.; Yang, P. Experimental Study on the Adsorption Performance of Metal–Organic Framework MIL-101 (Cr) for Indoor Toluene. *Buildings* **2025**, *15*, 2506. [CrossRef]
14. Kazemi, A.; Karbalaee Hosseini, A.; Ashourzadeh Pordsari, M.; Tamtaji, M.; Keshavarz, S.; Manteghi, F.; Tadjarodi, A.; Ghaemi, A.; Rohani, S.; Goddard, W.A. Enhancing CO_2 Selectivity in MOFs through a Dual-Ligand Strategy: Experimental and Theoretical Insights. *J. CO2 Util.* **2025**, *93*, 103035. [CrossRef]
15. Norouzbahari, S.; Mehri Lighvan, Z.; Ghadimi, A.; Sadatnia, B. ZIF-8@Zn-MOF-74 Core–Shell Metal–Organic Framework (MOF) with Open Metal Sites: Synthesis, Characterization, and Gas Adsorption Performance. *Fuel* **2023**, *339*, 127463. [CrossRef]
16. Ismail, M.; Bustam, M.A.; Kari, N.E.F.; Yeong, Y.F. Ideal Adsorbed Solution Theory (IAST) of Carbon Dioxide and Methane Adsorption Using Magnesium Gallate Metal-Organic Framework (Mg-Gallate). *Molecules* **2023**, *28*, 3016. [CrossRef]
17. Xie, L.; Ding, J.; Kong, X.; Qin, J.; Wang, J. Microwave-Assisted Synthesis of Mg-Gallate for Efficient CO_2 Capture. *Mater. Today Sustain.* **2023**, *22*, 100356. [CrossRef]
18. Chen, F.; Wang, J.; Guo, L.; Huang, X.; Zhang, Z.; Yang, Q.; Yang, Y.; Ren, Q.; Bao, Z. Carbon Dioxide Capture in Gallate-Based Metal-Organic Frameworks. *Sep. Purif. Technol.* **2022**, *292*, 121031. [CrossRef]
19. Wu, Y.; Fang, Y.; Fu, J.; He, L.; Kabtamu, D.M.; Matović, L.; Li, F.; Li, J. Optimized Scalable Synthesis and Granulation of MIL-88B(Fe) for Efficient Arsenate Removal. *J. Environ. Chem. Eng.* **2022**, *10*, 108556. [CrossRef]
20. Rozaini, M.T.; Grekov, D.I.; Bustam, M.A.; Pré, P. Shaping of HKUST-1 via Extrusion for the Separation of CO_2/CH_4 in Biogas. *Separations* **2023**, *10*, 487. [CrossRef]
21. Valekar, A.H.; Cho, K.-H.; Lee, U.-H.; Sun Lee, J.; Woong Yoon, J.; Kyu Hwang, Y.; Gwan Lee, S.; June Cho, S.; Chang, J.-S. Shaping of Porous Metal–Organic Framework Granules Using Mesoporous ρ-Alumina as a Binder. *RSC Adv.* **2017**, *7*, 55767–55777. [CrossRef]
22. Thakkar, H.; Eastman, S.; Al-Naddaf, Q.; Rownaghi, A.A.; Rezaei, F. 3D-Printed Metal–Organic Framework Monoliths for Gas Adsorption Processes. *ACS Appl. Mater. Interfaces* **2017**, *9*, 35908–35916. [CrossRef]
23. Askarieh, M.; Farshidi, H.; Rashidi, A.; Pourreza, A.; Alivand, M.S. Comparative Evaluation of MIL-101(Cr)/Calcium Alginate Composite Beads as Potential Adsorbents for Removing Water Vapor from Air. *Sep. Purif. Technol.* **2022**, *291*, 120830. [CrossRef]
24. Lee, D.W.; Didriksen, T.; Olsbye, U.; Blom, R.; Grande, C.A. Shaping of Metal-Organic Framework UiO-66 Using Alginates: Effect of Operation Variables. *Sep. Purif. Technol.* **2020**, *235*, 116182. [CrossRef]
25. Li, J.; Wang, X.; Liu, P.; Liu, X.; Li, L.; Li, J. Shaping of Metal–Organic Frameworks through a Calcium Alginate Method towards Ethylene/Ethane Separation. *Chin. J. Chem. Eng.* **2022**, *42*, 17–24. [CrossRef]
26. DeCoste, J.B.; Peterson, G.W. Preparation of Hydrophobic Metal-Organic Frameworks via Plasma Enhanced Chemical Vapor Deposition of Perfluoroalkanes for the Removal of Ammonia. *J. Vis. Exp. JoVE* **2013**, *80*, 51175. [CrossRef]
27. Effraimopoulou, E.; Jaxel, J.; Budtova, T.; Rigacci, A. Hydrophobic Modification of Pectin Aerogels via Chemical Vapor Deposition. *Polymers* **2024**, *16*, 1628. [CrossRef]
28. Greenspan, L. Humidity Fixed Points of Binary Saturated Aqueous Solutions. *J. Res. Natl. Bur. Stand. A Phys. Chem.* **1977**, *81*, 89–96. [CrossRef]
29. de Vargas Brião, G.; Hashim, M.A.; Chu, K.H. The Sips Isotherm Equation: Often Used and Sometimes Misused. *Sep. Sci. Technol.* **2023**, *58*, 884–892. [CrossRef]
30. Nuhnen, A.; Janiak, C. A Practical Guide to Calculate the Isosteric Heat/Enthalpy of Adsorption via Adsorption Isotherms in Metal–Organic Frameworks, MOFs. *Dalton Trans.* **2020**, *49*, 10295–10307. [CrossRef]
31. Li, J.; Yin, X.; Zhang, Z.; Jiang, Z.; Li, Z.; Li, Z.; Cheng, G. In Vitro Mineralization and Osteogenesis Effects of the Silk Fibroin Hydrogels Mineralized with SBF and $CaCl_2/Na_2HPO_4$ Methods. *Int. J. Biol. Macromol.* **2025**, *320*, 146051. [CrossRef]
32. Tran, H.Q.; ur Rehman, A.; Fioux, P.; Airoudj, A.; Vandamme, T.; Luchnikov, V. Formation of a Controllable Diffusion Barrier Layer on the Surface of Polydimethylsiloxane Films by Infrared Laser Irradiation. *ACS Appl. Mater. Interfaces* **2024**, *16*, 7983–7995. [CrossRef] [PubMed]
33. Tong, Z.; Chen, Y.; Liu, Y.; Tong, L.; Chu, J.; Xiao, K.; Zhou, Z.; Dong, W.; Chu, X. Preparation, Characterization and Properties of Alginate/Poly(γ-Glutamic Acid) Composite Microparticles. *Mar. Drugs* **2017**, *15*, 91. [CrossRef] [PubMed]
34. Fujiki, J.; Kajiro, H.; Takakura, Y.; Yajima, T.; Kawajiri, Y. Breakthrough Analysis for Parameter Estimation of CO_2 Adsorption on Pelletized Flexible Metal–Organic Framework. *Chem. Eng. J.* **2023**, *460*, 141781. [CrossRef]
35. Kannaka, S.; Ohmiya, A.; Ozaki, C.; Ohtani, M. Thermodynamic Analysis of Gate-Opening Carbon Dioxide Adsorption Behavior of Metal–Organic Frameworks. *Chem. Commun.* **2024**, *60*, 4171–4173. [CrossRef] [PubMed]
36. Lee, G.; Choi, D.; Oh, M. Activating the Gate-Opening of a Metal–Organic Framework and Maximizing Its Adsorption Capacity. *J. Am. Chem. Soc.* **2025**, *147*, 12811–12820. [CrossRef]

37. Peng, J.; Liu, Z.; Wu, Y.; Xian, S.; Li, Z. High-Performance Selective CO_2 Capture on a Stable and Flexible Metal–Organic Framework via Discriminatory Gate-Opening Effect. *ACS Appl. Mater. Interfaces* **2022**, *14*, 21089–21097. [CrossRef]
38. Cui, S.; Gu, Y.; Shao, Y.; Zhong, W. Experimental Research of Alkali Metals Modified Mg/DOBDC Metal Organic Framework as High Capacity CO_2 Adsorbent. *Sep. Purif. Technol.* **2024**, *331*, 125471. [CrossRef]
39. McDonald, T.M.; Mason, J.A.; Kong, X.; Bloch, E.D.; Gygi, D.; Dani, A.; Crocellà, V.; Giordanino, F.; Odoh, S.O.; Drisdell, W.S.; et al. Cooperative Insertion of CO_2 in Diamine-Appended Metal-Organic Frameworks. *Nature* **2015**, *519*, 303–308. [CrossRef]
40. Lin, J.-B.; Nguyen, T.T.T.; Vaidhyanathan, R.; Burner, J.; Taylor, J.M.; Durekova, H.; Akhtar, F.; Mah, R.K.; Ghaffari-Nik, O.; Marx, S.; et al. A Scalable Metal-Organic Framework as a Durable Physisorbent for Carbon Dioxide Capture. *Science* **2021**, *374*, 1464–1469. [CrossRef]
41. Gebremariam, S.K.; Varghese, A.M.; Ehrling, S.; Al Wahedi, Y.; AlHajaj, A.; Dumée, L.F.; Karanikolos, G.N. Hierarchically Porous Structured Adsorbents with Ultrahigh Metal–Organic Framework Loading for CO_2 Capture. *ACS Appl. Mater. Interfaces* **2024**, *16*, 50785–50799. [CrossRef]
42. Wang, S.-M.; Liu, H.-R.; Ni, S.; Yang, Q.-Y. A Structured Ultramicroporous Metal-Organic Framework for Carbon Dioxide Capture†. *Chin. J. Chem.* **2023**, *41*, 763–768. [CrossRef]
43. Lee, J.; Lee, H.; Tan, W.S.; Chuah, C.Y.; Tan, M.J.; Bae, T.-H.; Song, J. Enhancing CO_2 Capture Efficiency Using Optimized 3D-Printed Structured Adsorbents. *Sep. Purif. Technol.* **2025**, *361*, 131495. [CrossRef]
44. Lawson, S.; Griffin, C.; Rapp, K.; Rownaghi, A.A.; Rezaei, F. Amine-Functionalized MIL-101 Monoliths for CO_2 Removal from Enclosed Environments. *Energy Fuels* **2019**, *33*, 2399–2407. [CrossRef]
45. Zhou, Y.; Zhang, J.; Wang, L.; Cui, X.; Liu, X.; Wong, S.S.; An, H.; Yan, N.; Xie, J.; Yu, C.; et al. Self-Assembled Iron-Containing Mordenite Monolith for Carbon Dioxide Sieving. *Science* **2021**, *373*, 315–320. [CrossRef]
46. Zhang, J.; Feng, W.; Jin, J.; Mi, J.; Meng, H. Construction of Hydrophobic ALF@poly(Acrylates)-F Composite for Dynamic Adsorption of CO_2 from Humid Flue Gas. *Fuel* **2024**, *372*, 132269. [CrossRef]

Disclaimer/Publisher's Note: The statements, opinions and data contained in all publications are solely those of the individual author(s) and contributor(s) and not of MDPI and/or the editor(s). MDPI and/or the editor(s) disclaim responsibility for any injury to people or property resulting from any ideas, methods, instructions or products referred to in the content.